crystals

Article

Novel Detector Configurations in Cone-Beam CT Systems: A Simulation Study

Evangelia Karali , Christos Michail *, George Fountos, Nektarios Kalyvas and Ioannis Valais

Radiation Physics, Materials Technology and Biomedical Imaging Laboratory, Department of Biomedical Engineering, University of West Attica, Ag. Spyridonos, 12210 Athens, Greece; ekarali@uniwa.gr (E.K.); gfoun@uniwa.gr (G.F.); nkalyvas@uniwa.gr (N.K.); valais@uniwa.gr (I.V.)

* Correspondence: cmichail@uniwa.gr

Abstract: Cone-beam computed tomography (CBCT) has emerged in recent years as an adequate alternative to mammography and tomosynthesis due to the several advantages over traditional mammography, including its ability to provide 3D images, its reduced radiation dose, and its ability to image dense breasts more effectively and conduct more effective breast compressions, etc. Furthermore, CBCT is capable of providing images with high sensitivity and specificity, allowing a more accurate evaluation, even of dense breasts, where mammography and tomosynthesis may lead to a false diagnosis. Clinical and experimental CBCT systems rely on cesium iodine (CsI:Tl) scintillators for X-ray energy conversion. This study comprises an investigation among different novel CBCT detector technologies, consisting either of scintillators (BGO, LSO:Ce, LYSO:Ce, LuAG:Ce, CaF_2:Eu, $LaBr_3$:Ce) or semiconductors (Silicon, CZT) in order to define the optimum detector design for a future experimental setup, dedicated to breast imaging. For this purpose, a micro-CBCT system was adapted, using GATE v9.2.1, consisting of the aforementioned various detection schemes. Two phantom configurations were selected: (a) an aluminum capillary positioned at the center of the field of view in order to calculate the system's spatial resolution and (b) a breast phantom consisting of spheres of different materials, such that their characteristics are close to the breast composition. Breast phantom contrast-to-noise ratios (CNRs) were extracted from the phantom's tomographic images. The images were reconstructed with filtered back projection (FBP) and ordered subsets expectation-maximization (OSEM) algorithms. The semiconductors acted satisfactorily in low-density matter, while LYSO:Ce, $LaBr_3$:Ce, and LuAG:Ce presented adequate CNRs for all the different spheres' densities. The energy converters that are presented in this study were evaluated for their performance against the standard CsI:Tl crystal.

Keywords: cone-beam CT (CBCT); single crystals; scintillators; semiconductors; modulation transfer function (MTF)

check for updates

Citation: Karali, E.; Michail, C.; Fountos, G.; Kalyvas, N.; Valais, I. Novel Detector Configurations in Cone-Beam CT Systems: A Simulation Study. *Crystals* **2024**, *14*, 416. https://doi.org/10.3390/cryst14050416

Academic Editor: Yutaka Fujimoto

Received: 2 April 2024
Revised: 23 April 2024
Accepted: 27 April 2024
Published: 29 April 2024

1. Introduction

Breast imaging constitutes a powerful diagnostic tool in the area of the prevention and early diagnosis of most breast pathologies. Until recently, breast examination has relied on mammography and tomosynthesis [1]. However, during these imaging protocols, the breast is compressed in a painful manner, while there is an increased probability of a false diagnosis in the case of dense breasts. Cone-beam computed tomography (CBCT) is capable of overcoming breast compression by using a comfortable imaging technology [2]. Furthermore, it presents images with high sensitivity and specificity that lessen the possibility of a false diagnosis or even reduce the need for a breast biopsy [1]. Additionally, quantitative material decomposition, including the quantification of contrast agents, electron density, and virtual monoenergetic images, is also applicable to CBCT [3,4].

CBCT technology relies on a detector technology that uses a scintillator (e.g., cesium iodine doped with thallium CsI:Tl) for X-ray energy conversion to light followed by common light converters to electric pulses. CsI doped with Tl ions presents a high light yield of more than 60,000 ph/MeV at room temperature [5]. Its light emission band (maximum at 560 nm) is satisfactory when combined with the spectral sensitivity of photodiodes [6]. CsI:Tl presents a rather slow response to X-ray photons. Its decay time constant (0.6–0.9 µs) can be inadequate for high photon counting X-ray imaging applications [6], whereas, even when doped with Tl ions, it remains a hygroscopic scintillator. The latter deteriorates its applications in high humidity conditions [7,8]. Moreover, CsI:Tl exhibits high levels of afterglow in its scintillation decay that produces image blurring in high-speed imaging applications [9].

Scintillation detector technology is characterized as an indirect photon energy conversion method. In general, scintillators attached to a photomultiplier tube (PMT) or an avalanche photodiode matrix (silicon photomultipliers-SiPMs) form an indirect light-to-signal conversion method. Direct conversion can be performed by utilizing semiconductor detectors. Scintillators used commonly in X-ray tomography are cadmium tungstate ($CdWO_4$), lead tungstate (PWO), CsI:Tl, and lutetium yttrium orthosilicate doped with cerium (LYSO:Ce), while among semiconductor detectors, cadmium zinc telluride (CZT) dominates [10]. In general, semiconductors are in favor for diagnostic purposes since the conversion of X-ray to electric pulse is performed directly without extra hardware, as in scintillators that are connected to light and to electric pulse converters (e.g., PMTS or SiPMs). Thus, any additional electronic or thermal noise is avoided. This allows semiconductors to improve image spatial resolution and image contrast- (or signal-) to-noise ratios (CNR or SNR) under low-dose examinations [11–13] where conventional imaging techniques suffer from high noise levels that degrade image quality.

Image quality depends on the SNR or CNR. Noise reduction improves the detection of low-contrast objects in the image, i.e., a soft tissue tumor in a dense breast and/or low-contrast masses. Noise is inversely proportional to the square root of the number of photons collected for image formation. The SNR (or CNR) can, therefore, be improved either by increasing the number of incident photons (e.g., through a higher mAs value), together with an increase in the dose to the patient, or by using a larger portion of the photons reaching the detector, which in turn increases the detective quantum efficiency (DQE) [14]. Higher DQE improves image quality without increasing the dose to the patient [12]. DQE can also be improved by using thicker detectors or materials with higher attenuation coefficients (μ). The latter increases with increasing atomic number, which in turn increases the physical density of the absorbing material [15,16].

In this research, the performance of a micro-CBCT system was evaluated, using Monte Carlo methods for possible applications in a dedicated CBCT breast imaging system. The scanner imaging efficiency was evaluated under a wide range of novel CBCT/scintillator detector configurations in order to estimate the performance of the optimum combination. Scintillators and semiconductors were investigated as possible X-ray energy converters. The scintillators that were examined were bismuth germanate (BGO), lutetium oxyorthosilicate doped with cerium (LSO:Ce), LYSO:Ce, CsI:Tl, lutetium aluminum garnet doped with cerium (LuAG:Ce), and lanthanum bromide doped with cerium ($LaBr_3$:Ce). Furthermore, silicon and CZT semiconductors were also evaluated. Clinical and experimental X-ray systems commonly use LYSO:Ce [17], while LSO:Ce and BGO can be found in clinical and experimental γ-ray applications [18]. These materials are dense (they all exhibit density values around 7 g/cm^3) with sufficient light output (BGO 30% and LSO:Ce, LYSO:Ce 85% of NaI:Tl scintillator) [19]. LuAG:Ce attracts great scientific interest because of its relatively high density (6.67 g/cm^3 [20]), satisfactory light output, and very fast response to X-radiation (55 ns). In addition, the wavelength (526 nm) of the secondary photons emitted by LuAG:Ce is transformed with high efficiency to electric pulses upon coupling with avalanche photodiode arrays [21]. Moreover, although $LaBr_3$:Ce is hygroscopic, it receives great scientific attention because of its rapid response to incident photons (~20 ns [22]). Likewise, CZT is a material that is under investigation as an adequate X-ray CT system detector since it presents decreased electronic noise (a magnitude of nA [23]) and an increased signal-to-noise ratio [11,24–26].

The high density and the high effective atomic number (Zeff) of the examined materials (higher than that of CsI:Tl crystal) improve DQE and can produce images of better image quality without a further increase in the dose levels. Novel CBCT detector configurations that can increase the SNR, while keeping the dose to the patient as low as possible, raise a high scientific interest [27].

Thus, this study aims to investigate promising scintillating materials that can increase contrast-to-noise ratios, in comparison to the imaging result of the standard CsI:Tl crystal.

2. Materials and Methods

In this study, an X-ray cone-beam micro-CT system, shown in Figure 1, was simulated, by using an X-ray source (micro-focus X-ray source) with an emission angle of 6.8°. The energy spectrum of the source ranges from 10 to 40 keV. The object under examination is placed on a 360° rotating table (with respect to the vertical axis), which is located at a distance of 15 cm from the source. The distance between the detector and the source is 300.05 cm. The detector consists of either a semiconductor or a scintillator, and it is discretized into 100 × 100 pixels. Each detector has dimensions of 50 mm × 50 mm × 1 mm, thus the resulting detector pixel dimensions are 0.5 mm × 0.5 mm × 1 mm. The magnification is 1.07. The system was simulated by using GATE v9.2.1 [28].

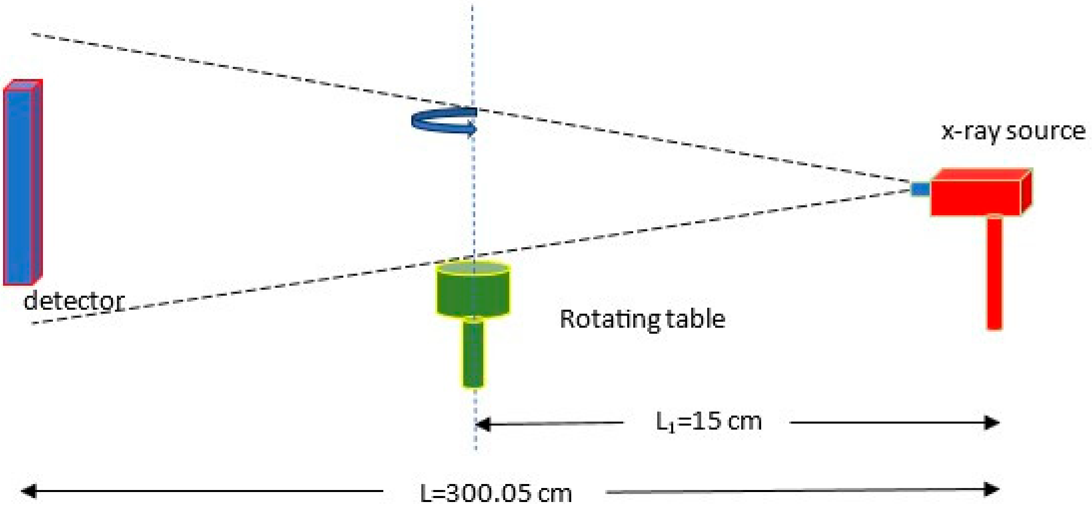

Figure 1. Schematic diagram of the X-ray cone-beam micro-CT system.

GATE is based on the GEANT4 simulation tool that is used mainly in high-energy physics [28]. It actually stands for the GEANT4 application for tomographic emission. It is an advanced Monte Carlo simulation software that can be used to simulate radiation interactions (attenuation, scatter, absorption of photons), detector configurations, acquisition protocols, and signal processing during a nuclear medicine imaging examination [29,30].

Thus, GATE is a powerful tool for assisting the design of new imaging systems, optimizing examination protocols, and investigating novel detection and signal processing methodologies. The latest version of GATE incorporates simulation routines for X-ray computed tomography applications [31].

The micro-CBCT detection system was simulated consisting of six different scintillators, namely, BGO, LSO:Ce, LYSO:Ce, CsI:Tl, LuAG:Ce, and $LaBr_3$:Ce. In addition, silicon and CZT semiconductors were also examined. In Tables 1 and 2, important properties of the aforementioned materials are presented. In general, materials with short decay times and high light output are preferable in medical imaging. Each detector is coupled to the same electronic signal processing. A simple pulse analysis case with an energy threshold of 10 keV has been chosen to be simulated.

The purpose of this study was to assess the image quality of a micro-CBCT system. Image quality can be quantified by the imaging device's spatial resolution and contrast-to-noise ratios. Spatial resolution usually is determined by using point (or line) cold sources, like a metallic capillary [16,32,33]. In order to assess different aspects of a detector scheme's imaging efficiency, two phantom geometries (Figure 2) were simulated. Simulation results of the first phantom, namely, an aluminum capillary of 1 mm in diameter and 20 mm long (Figure 2a), were used to evaluate the spatial resolution of each detector scheme. Scatter effects were not simulated. The second phantom in our simulation was a breast phantom (Figure 2b), in order to investigate the contrast-to-noise ratio in a strong scattering environment (water) for each detector technology. The breast phantom consists of a cylindrical container filled with distilled water. Inside this water tank, four "cold" spherical sources of aluminum, plastic, glass, and bone tissue have been placed. The cylindrical container has a radius of 8 mm and a height of 20 mm.

Table 1. Properties of scintillation materials under investigation [34–36].

Scintillating Materials Properties	BGO	LSO:Ce	LYSO:Ce	LuAG:Ce	CsI:Tl	$LaBr_3$:Ce
Light output (%NaI)	30	85	85	66	45	166
Decay time (ns)	60/300	40	53	70	1000	26
Emission peak (nm)	480	420	420	535	550	380
Refraction index	2.15	1.82	1.81	1.84	1.79	2.05
Density (g/cm^3)	7.13	7.35	5.37	6.67	4.51	5.23
Z_{eff}	75	66	66	61	54	46.9

Table 2. Properties of examined semiconductor detectors [37].

Properties	Si	CZT
Energy gap (ev)	1.12	1.4–2.2
Average energy/e-h coupling	3.61	4.67
Dielectric constant	11.9	10.9
Density (g/cm^3)	2.3	5.8
Atomic number	14	50

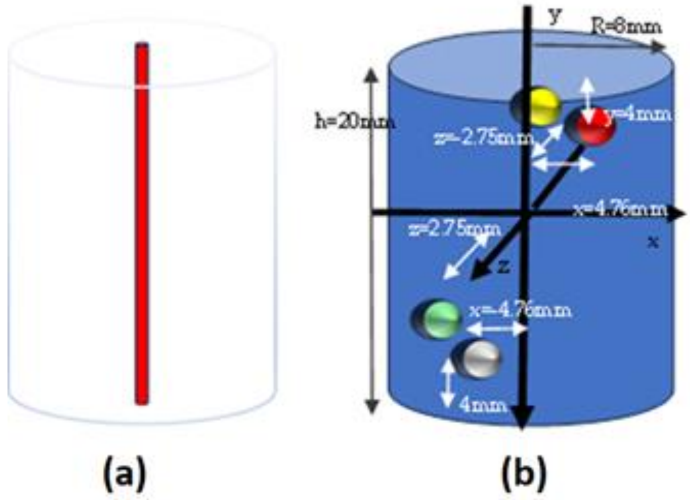

Figure 2. The simulated phantom geometries are shown. In (**a**), the simulated geometry of an aluminum capillary is displayed and, in (**b**), the schematic geometry of a breast phantom. The aluminum capillary is 20 mm in height and 1 mm in diameter. The breast phantom consists of a water cylinder with a radius of 8 mm and a height of 20 mm. The water cylinder contains four "cold" sources (spheres) made of aluminum (red), polyvinyl chloride (PVC) (yellow), glass (green), and bone tissue (silver). The spheres are all 1 mm in diameter and are placed inside the water cylinder as shown in Figure 2b.

Tomographic images of each phantom were reconstructed with two different algorithms: the analytical, filtered back projection (FBP) technique [10], and the statistical, ordered subsets expectation-maximization algorithm (OSEM) [38]. Reconstructed images' size was 128 × 128 pixels. FBP reconstructed images represent an area of 25 mm × 25 mm, while OSEM reconstructed images correspond to an area of 17 mm × 17 mm. The FBP reconstruction algorithm assumes a parallel beam geometry, which expands the camera's field of view. OSEM is applied by considering the actual fan beam geometry that is applied for a 2D reconstruction process in a cone-beam geometry.

FBP is based on the hypothesis that the 1D acquisition data Fourier transform equals the 2D reconstructed image Fourier transform. FBP was implemented by applying a Hamming window in order to avoid blurring phenomena in reconstructed images while, at the same time, reducing high-frequency image noise and improving SNR.

On the other hand, OSEM represents a speedup version of the expectation-maximization maximum likelihood (EMML) algorithm [39] that assumes that acquired data follow a Poisson statistic. Iterative algorithms in general produce images with better CNR or SNR values and with improved spatial resolution, free from the artifacts of analytical reconstruction [40]. To succeed with this, iterative methods usually rely on a linear relation between acquired data y and image x, according to the following equation:

$$y = A^T x \tag{1}$$

where A is the system or probability matrix, a matrix variable that models all the physical phenomena during the data acquisition process, i.e., the X-ray scatter and attenuation, as well as scanner geometrical characteristics (angle of rotation, object-to-detector distance, distance from the object to X-ray source, detector's pixels number, detector pixel size, image size, image pixel size, angle of X-ray emission). Element a_{ij} of the matrix A represents the probability of an X-ray passing from image pixel i being detected by detector pixels j that define LOR j (LOR-line of response). Since A is not quadratic, A^{-1} cannot be calculated; thus, Equation (1) cannot be directly solved to find image x. By multiple iterations based on specific objective functions, relative to the data acquisition of physical phenomena, iterative techniques are able to reach an optimum image representation of the object under study, to produce the optimum solution of Equation (1) [41].

OSEM is based on the assumption that the collected data follow a Poisson distribution with mean value $\sum_{i=1}^{N} a_{ij} x_i$, where N is the total image pixel number. OSEM speeds up EMML by dividing into subsets the acquired data y so that one full iteration is fulfilled when all data subsets are used to reconstruct image x.

There is no gold standard on the choice of subsets; that is, they can be sequentially ordered with no overlap between them or they can be overlapping subsets with increasing size, etc. The iterative step of OSEM in kth iteration for subset n is as follows:

$$x_i^k = \frac{x_i^{k-1}}{\sum_{j \in S_n} a_{ij}} \sum_{j \in S_n} \frac{a_{ij} y_j}{\sum_{i=1}^{N} a_{ij} x_i^{k-1}} \tag{2}$$

The system matrix was derived from an analytical formula as the area of intersection between two lines of response. In Figure 3, the hall method is presented with the camera at a random rotation angle in relation to the object under investigation. Only scanner geometrical characteristics were taken into account.

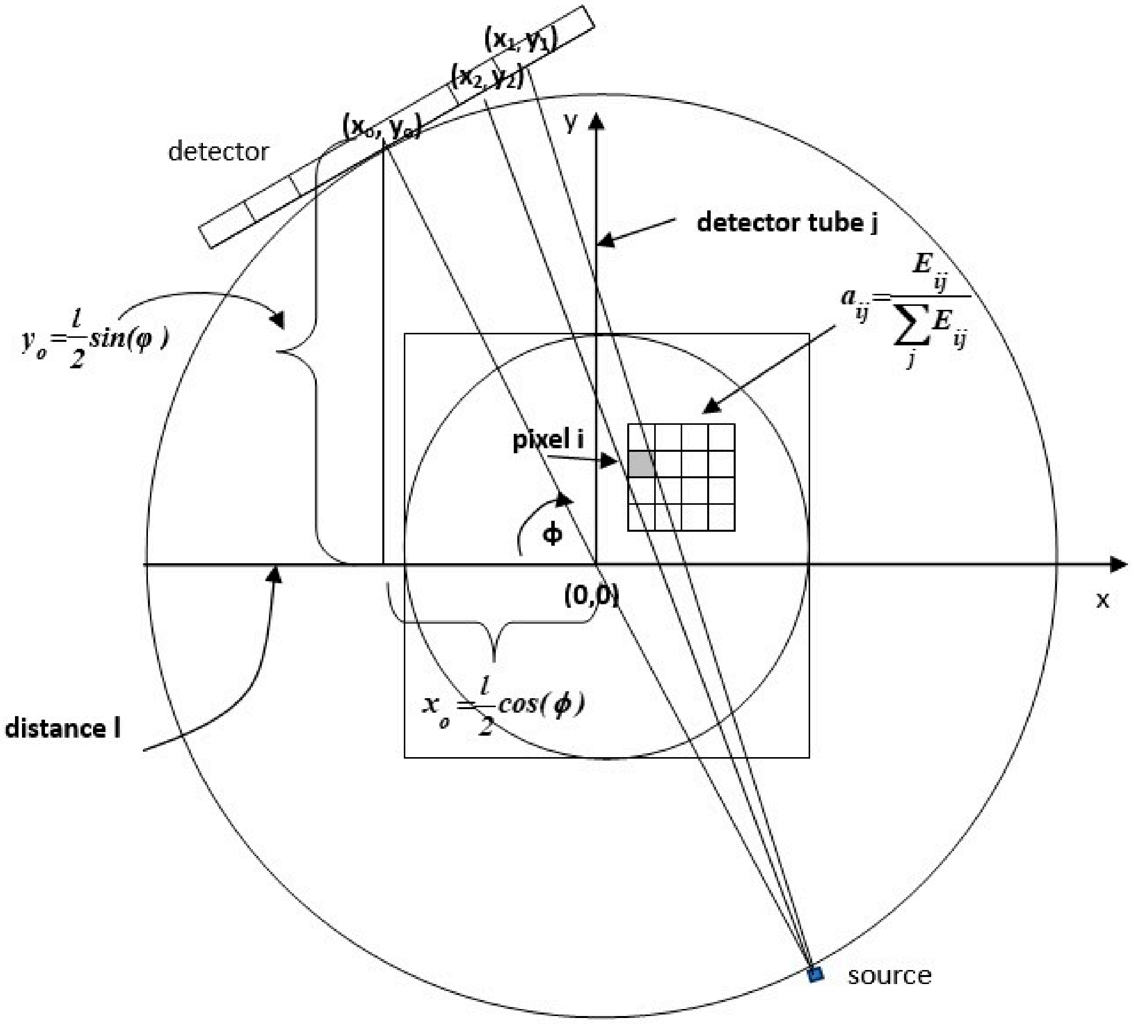

Figure 3. A schematic view of the system matrix element calculation (*Eij* are areas of intersections between two detector lines of response and pixel *i*). The figure presents the micro-CBCT system configuration when the table is rotated at a random angle (φ). *I* represent the detector to source distance, (x_o, y_o) are the coordinates of the detector center, (x_1, y_1) and (x_2, y_2) are the coordinates of two randomly chosen neighboring detector pixels. a_{ij} represents the system matrix element corresponding to the area of intersection. E_{ij} of pixel *i* with detector tube *j* is defined between neighboring lines of response, originating from detector pixels with coordinates (x_1, y_1) and (x_2, y_2).

3. Results

Simulation data are acquired by a table rotation of 1 °/s for 360°. The source and the detector are stationary and facing each other. The maximum activity of the source was 350 kBq, corresponding to 9.46 μCi.

As far as the aluminum capillary is concerned, it was used to extract the point spread function (PSF) system response. The capillary was simulated with air in the surroundings. Simulated data (number of X-ray photons being absorbed in the detector) were stored in sinogram format. One hundred 2D sinograms were generated. Each sinogram was referred to a specific detector pixels' row. Thus, each sinogram 2D matrix contained the number of photon interactions of every pixel detector in a specific detector row and in every rotation angle. To extract the PSF (the capillary profile along a tomographic plane), the 2D sinograms were reconstructed into 2D tomographic images. A total of 100 tomographic images were created. The tomographic image #50, out of 100 in total, which showed the cross-section of the capillary at a height of 10 cm, was chosen. The midrow # 50 of the aforementioned two-dimensional cross-section was used. Figure 4 shows a superimposition of the source profile, for the specific line of cross-section 50, for all the detection patterns. The image source was reconstructed with FBP (applied as explained in the previous section) (Figure 4a) and OSEM (Figure 4b). OSEM is applied by dividing the dataset into 24 subsets and repeating the iterative procedure two times. The minimum of the source profile is subtracted and then the profile is normalized.

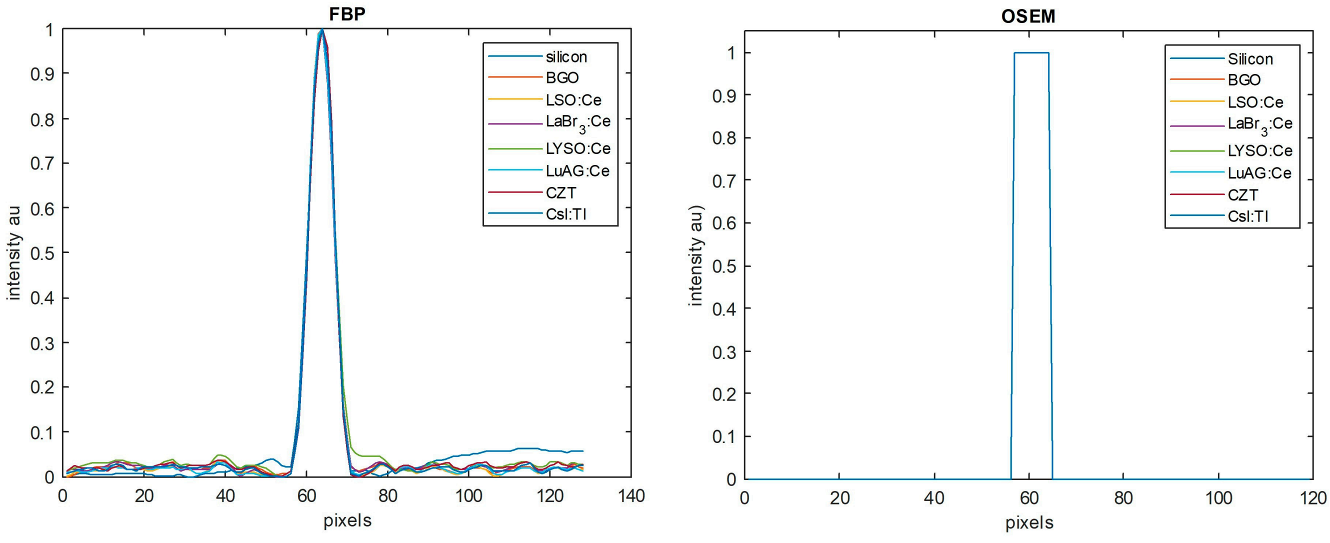

(a) **(b)**

Figure 4. A superimposition of the source profile, for the specific line of cross-section 50 and for all the detection patterns. The capillary image was reconstructed with (**a**) FBP and (**b**) OSEM (24 subsets, 2 iterations) in a 128 × 128 pixels matrix.

Figure 5 shows the modulation transfer function (MTF) [42], which is actually the Fourier transform of Figure 2. MTFs for each detector array are superimposed. No differentiation is present among the different detector set-ups as far as the reconstruction procedure with FBP is concerned. The resolution was still (at 10% of MTF) 1.19 cycles/mm for all detector arrays.

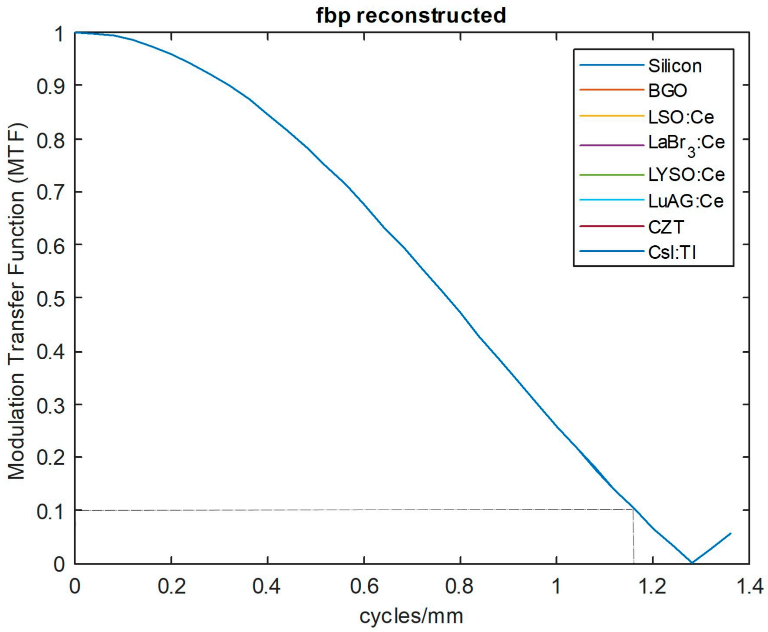

Figure 5. A superimposition of MTFs for each CBCT/detector combination. The image source was reconstructed with FBP. The gray dashed line denotes the MTF at 10%.

Figure 6 presents the superimposition of each detector scheme's MTFs where the image source was reconstructed with OSEM. The top row shows MTF curves for the image source reconstructed with OSEM by using 9 subsets, the middle row by using 15 subsets, and the bottom row by using 24 subsets. It can be concluded from Figure 6 that the number of subsets does not make a considerable contribution to increasing the spatial resolution. The number of iterations has the most significant role, resulting in a better spatial resolution. Thus, after three iterations of OSEM by using 24 subsets, the spatial resolution is significantly improved to almost 1.5 cycles/mm. The image size in both FBP and OSEM reconstruction was 128 × 128 pixels.

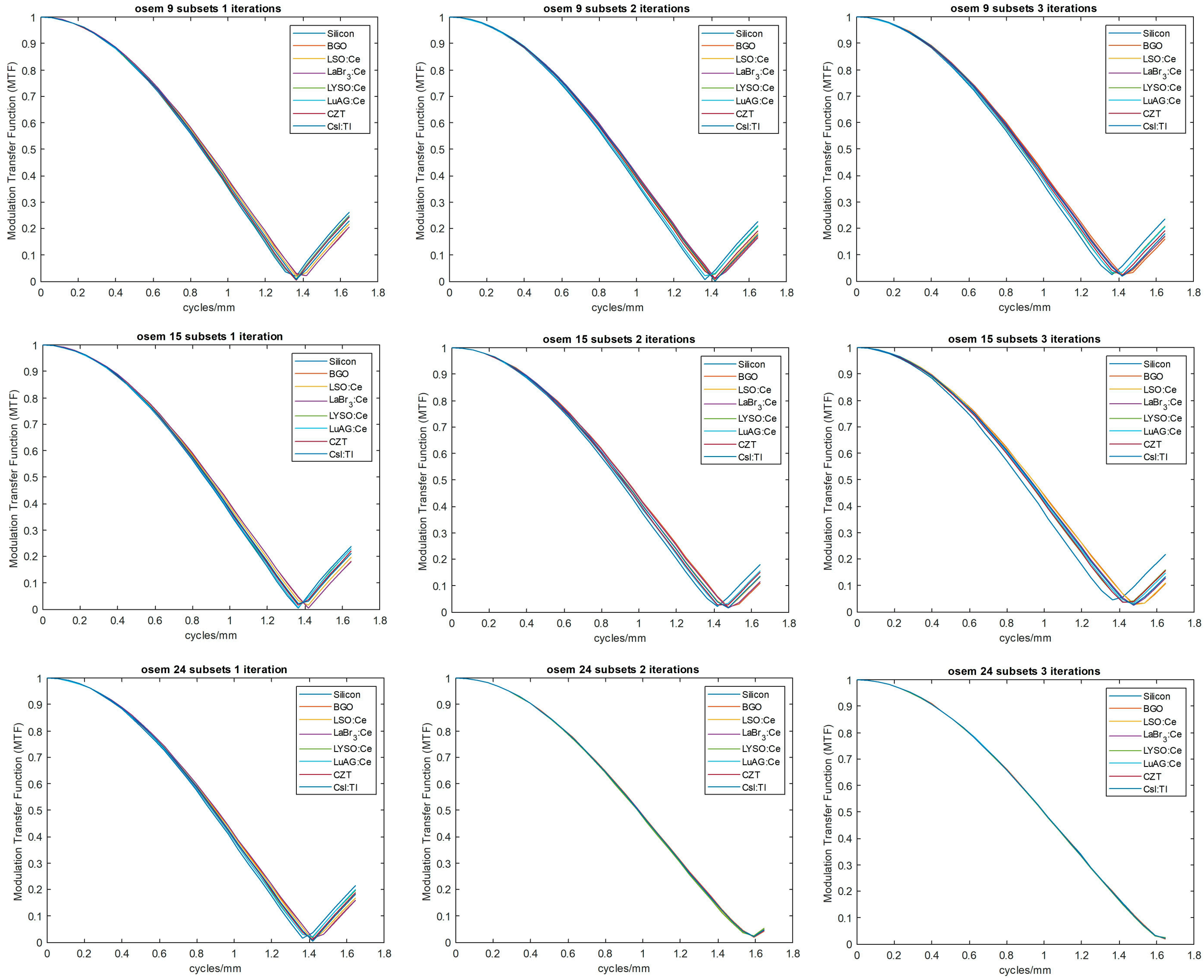

(a) **(b)** **(c)**

Figure 6. A superimposition of each detector configuration's MTFs, where the image source was reconstructed with OSEM (the top row shows MTF curves for the image source reconstructed with OSEM by using 9 subsets, the middle row by using 15 subsets, and the bottom row by using 24 subsets) after (**a**) 1 iteration, (**b**) 2 iterations, and (**c**) 3 iterations.

The image of the capillary for the LYSO:Ce (left), CZT (center), and $LaBr_3$:Ce (right) detectors at a 36° rotation is presented in Figure 7. Figure 8 shows the capillary tomographic images (slice 50) for the LYSO:Ce detector (left), the CZT semiconductor (center), and the

LaBr$_3$:Ce scintillator (right) reconstructed with FBP (top row) and OSEM (bottom row), using 24 subsets and two iterations.

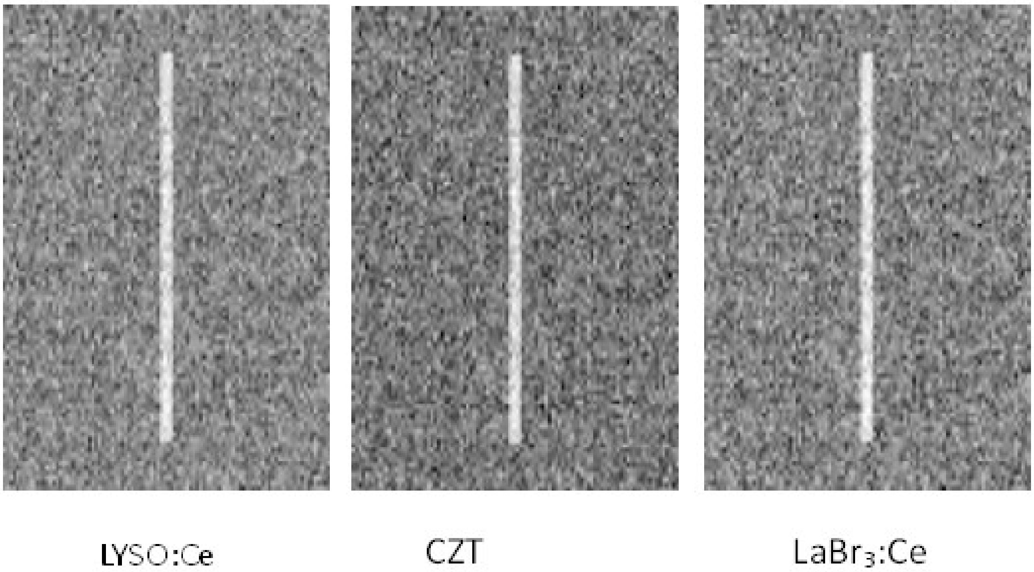

Figure 7. The views of the aluminum capillary in the air for three detection materials at a 36° rotation angle.

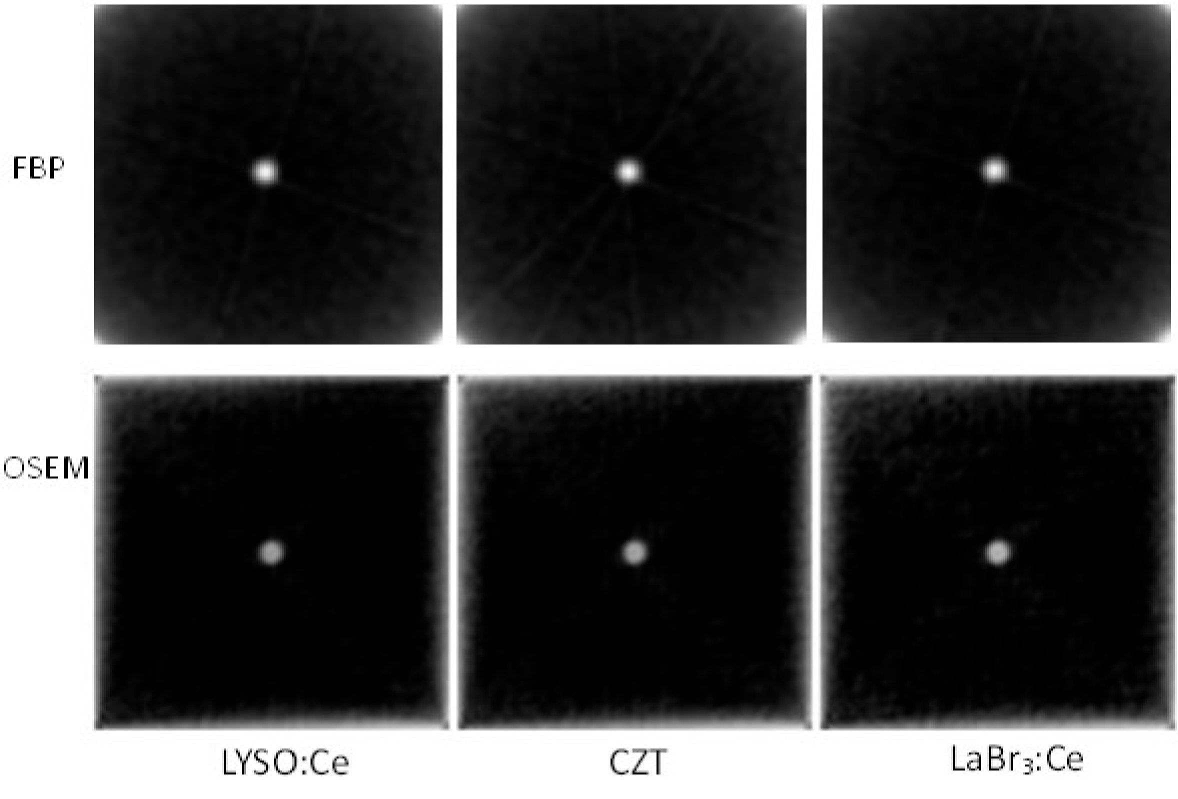

Figure 8. The capillary tomographic images (slice 50) for the LYSO:Ce detector (**left**), the CZT semiconductor (**center**), and the LaBr$_3$:Ce scintillator (**right**) reconstructed with FBP (**top row**) and OSEM (**bottom row**) by using 24 subsets and 2 iterations.

Furthermore, regions of interest (ROIs) within the breast phantom consisting of four spheres (simulated with materials of different densities (aluminum, plastic, glass, and spinal bone tissue)), in a water cylinder, were selected. ROIs were chosen from the reconstructed images (cross-sections 26 and 76) with FBP and OSEM (24 subsets, two iterations). Cross-section 26 contains the two aluminum and plastic cold sources, and cross-section 76 contains the glass and spine bone spheres. Three background-noise regions within the camera's field of view were also examined. The mean background luminance $M_{background}$ and standard deviation of the three noise regions were calculated. The size of the ROIs was 8 × 8 pixels, placed in the centers of the four spheres.

Information regarding the regions of interest concerning the spheres was used to calculate each sphere's average brightness value, M_{object}. From the background ROIs, the average background value $M_{background}$ was extracted and subtracted from M_{object}. The contrast-to-noise ratios (CNRs) [42] were then calculated based on the following equation:

$$CNR_{object} = \frac{M_{object} - M_{background}}{\sigma_{background}} \tag{3}$$

Table 3 shows the CNR coefficients for the eight different probe arrangements and for each sphere for cross-sections 26 and 76 reconstructed with FBP and OSEM.

Figure 9 presents the tomographic images (128 × 128 in pixels) of the four spheres, namely, slice 26 and slice 76. The top row shows reconstructed images from data acquired with the LYSO:Ce crystal, the middle row with the CZT semiconductor, and the bottom row with the $LaBr_3$:Ce scintillator. The two columns on the left present FBP reconstruction, while the two columns on the right present images reconstructed with OSEM (24 subsets, two iterations).

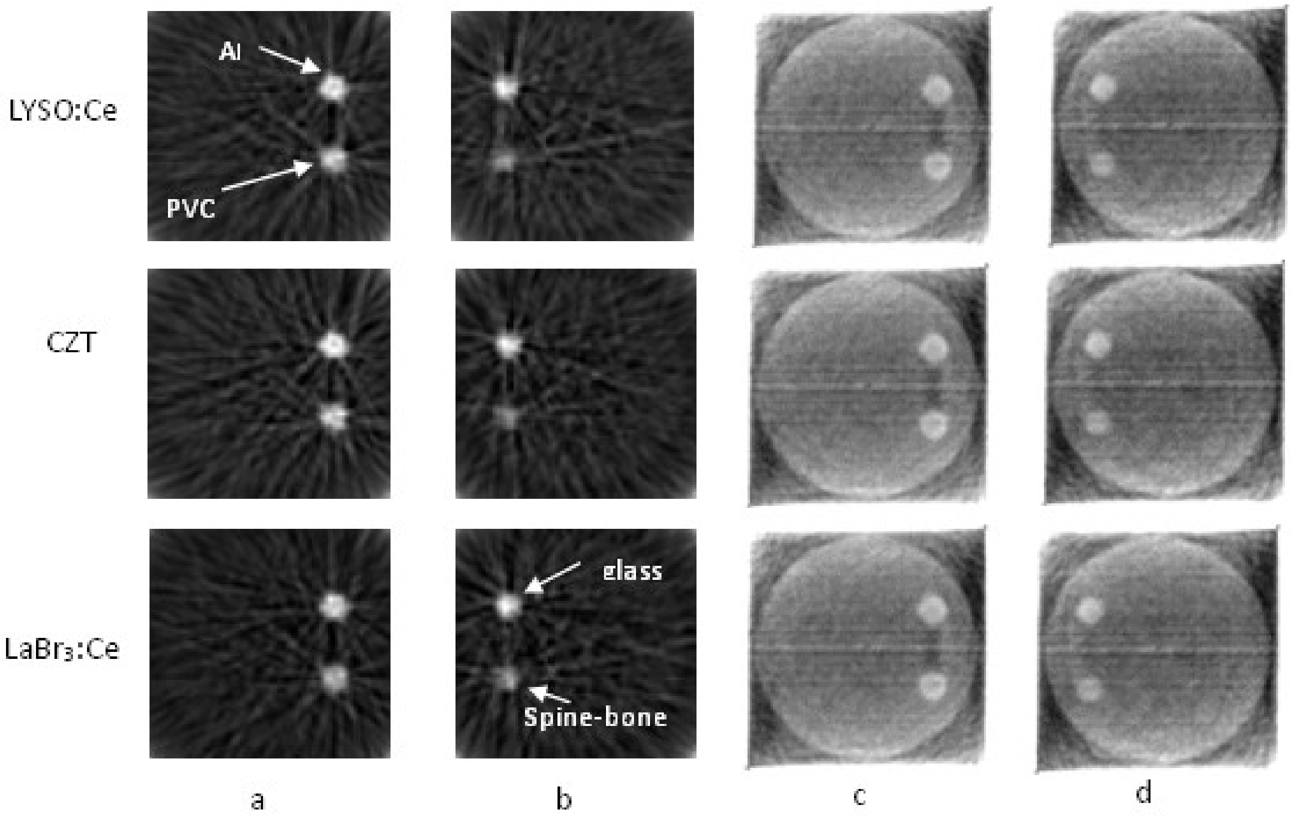

Figure 9. Tomographic images of the four spheres, namely, slice 26 and slice 76. The top row shows reconstructed images from data acquired with the LYSO:Ce crystal (top row), the CZT semiconductor (middle row), and the $LaBr_3$:Ce scintillator (bottom row). (**a**,**b**) stand for FBP reconstruction, while (**c**,**d**) columns present images reconstructed with OSEM (24 subsets, 2 iterations).

Table 3. The CNR for the breast phantom spheres and for data acquired from the detector schemes under investigation.

	FBP				**OSEM**			
Detector Materials	**CNR_{Al}**	**CNR_{PVC}**	**CN_{glass}**	**CNR_{bone}**	**CNR_{Al}**	**CNR_{PVC}**	**CN_{glass}**	**CNR_{bone}**
CsI:Tl	**12.5677**	**10.2876**	**5.4582**	**2.2838**	**16.2694**	**15.2954**	**7.9191**	**4.5620**
BGO	13.6643	11.1720	4.9783	2.3314	20.3974	19.4525	9.8848	5.9640
CZT	11.6429	9.6542	6.6954	2.8265	15.2184	14.1728	8.6443	4.9778
$LaBr_3$:Ce	13.4469	11.1696	6.6189	3.5607	20.4403	19.4915	8.8816	5.2766
LSO:Ce	12.4842	10.5126	5.8054	2.5998	12.2756	11.3903	8.1536	4.6478
LuAG:Ce	13.1741	11.1357	6.2501	2.8842	15.7086	15.0080	7.5545	4.2416
LYSO:Ce	14.5738	12.0385	4.2762	2.2064	21.1344	20.1747	9.5491	5.7420
Silicon	12.0868	9.0101	5.9142	2.6967	11.0312	10.3268	5.9028	2.5920

4. Discussion

By observing Table 3, under simulation assumptions, all the CNRs are acceptable for aluminum, plastic, and glass spheres. This is also the case for all detection schemes and for both FBP and OSEM reconstruction procedures, i.e., CNR > 3 (Rose criterion) [41]. The spine bone (the less dense material) sphere is barely detected, presenting CNRs above the Rose criterion for FBP images. However, using energy converters denser than CsI:Tl, such as CZT, $LaBr_3$:Ce, and LuAG:Ce, the bone sphere's CNR approaches the Rose criterion of adequate detection. OSEM reconstruction enhances contrast-to-noise ratios, and almost all spheres' CNRs are acceptable. Furthermore, the denser materials show increased CNR values for all four spheres in comparison to the CsI:Tl scintillator. LuAG:Ce and silicon seem to perform better in conjunction with the FBP reconstruction process.

Lately, there has been an increased research interest [3] and clinical evaluation of cone-beam CT systems, dedicated to breast imaging. Cone-beam CT avoids tissue overlapping and provides a more sensitive evaluation for dense breasts (mean density d = 1.1 g/cm^3 [43]). In this study, CNR values can be characterized as significantly high. An X-ray mammograph image was also simulated. CNRs values, for detector configurations based on CsI:Tl crystal, were as follows: CNR_{Al} = 7.4263, CNR_{PVC} = 6.5323, CNR_{glass} = 6.0179, and CNR_{bone} = 3.9641. These values are lower than CNR values for aluminum, PVC, and glass obtained with the micro-CBCT system for the same detector material. CNR_{bone} is also low in comparison with the $CNRs_{bone}$ obtained by micro-CBCT for images reconstructed with OSEM. This confirms the increase in the system sensitivity of the simulated micro-CBCT system [1].

According to Table 3, and under the simulation assumptions, semiconductors tend to have more satisfactory CNRs in the bone sphere than CsI:Tl. The above findings are indicative of the increased scientific interest in the CZT detector's evaluation for CT systems, especially in the area of photon counting CT [44,45]. In this context, a previous study, evaluating two CBCT system configurations (one with a CsI:Tl flat panel detector, while the other was based on a CZT semiconductor) resulted in a CNR increase of 1.48 for microcalcifications and 1.85 for iodine contrast enhancement, when CZT-based configuration was used, instead of the common CsI:Tl scintillator [46].

In the literature, there are a few studies that investigate the influence of the incorporation of CZT detectors in X-ray CT scanning protocols on CNR. All these studies report an increase in the CNR in the range from 1.3 to 1.4 [47].

$LaBr_3$:Ce and LuAG:Ce scintillators are in the spotlight of material research, due to their fast response to the incident radiation and the light output, especially in the case of $LaBr_3$:Ce compared to the NaI:Tl crystal. LuAG:Ce is a very promising scintillator as far as the light output is concerned, while at the same time, it is preferably combined with SiPMs. The use of SiPMs in the detector array reduces electronic noise, increases the energy resolution, and reduces the cost of the detector system relative to the use of a photomultiplier. SiPMs are now established in clinical systems and facilitate the development of digital imaging detectors. The LYSO:Ce crystal is today at the heart of clinical and international research activity [7,25].

Based on the above findings, photon energy converters like CZT, LYSO:Ce, $LaBr_3$:Ce, and LuAG:Ce could be potentially used as alternatives to CsI:Tl crystal in future experimental CBCT applications.

Aluminum is a dense material with a high attenuation coefficient in the energy range under examination. In addition, aluminum's capillary diameter is bigger than the detector pixel size; thus, it is detected equally satisfactorily by all detector setups.

The breast phantom investigated in this study simulated three types of tissue: fat, muscle, and bone. Adipose tissue is simulated by PVC (plastic), and muscle is simulated by water. At energies below 40 keV, the fatty tissue is clearly visible compared to the muscle tissue, but the radiation dose absorbed by the body under examination increases. Therefore, X-ray photons in clinical systems approach energies of 40 keV, which are the upper limit for distinguishing the two tissues from each other.

As far as noise artifacts [45,48] are concerned, in Figure 9, the beam hardening effect as a product of FBP reconstruction is clearly visible, hindering the visibility of low-contrast objects in the vicinity of high-Z objects (aluminum and glass). This can be avoided by using iterative reconstruction algorithms, as can be inferred from Figure 9b. The relatively high simulated pixel size of 0.5 mm may also enhance the partial volume effect artifact, especially in FBP images. The effect of the latter may be reduced by simulating with a smaller pixel size or using an iterative algorithm.

Although the main interaction of X-ray energy impinging on the breast phantom is scattering, the lower X-ray energies, close to 10 KeV, demonstrate an increased probability of direct absorption due to the photoelectric effect. The above suggests an increased contribution of scattering in the presented data. The use of a larger phantom would change the scatter energy distribution incident on the detector and is expected to reduce the image clarity for all detector configurations. All images were simulated under conditions of intense noise and in an intense scattering environment, such as the container of water, under low X-ray source activity exposure. The bone sphere is hard to distinguish, mainly in FBP-reconstructed images. Furthermore, compared to the three other materials, it has the lowest density of 1.4 g/cm^3 (GATE data [28]) (d_{Al} = 2.7 g/cm^3, d_{PVC} = 1.65 g/cm^3, d_{glass} = 2.5 g/cm^3). This is also shown by the CNR ratios, which for the bone "source", can be above the Rose criterion.

Breast phantom proportions do not reflect a real human breast volume. They reflect a small area that resembles breast tissue. It is designed so as to assess detector material effectiveness to distinguish between different structures (with dimensions close to the presented micro-CBCT system's spatial resolution) in a small area of simulated breast tissue.

OSEM was implemented by adapting a sequential, non-overlapping technique for subsets' selection. Images are obtained according to one subset of the data and used as an initial solution, input to the reconstruction process of the next subset. When all subsets have been used, one full iteration of the algorithm is completed. OSEM is an accelerated version of EMML. Two full iterations of OSEM with 24 subsets are not equal to two full iterations of EMML. The latter needs an optimum of 50 iterations to reach an acceptable result [39].

Finally, iterative techniques, like OSEM, improve the CNR, mostly because they produce images with lower noise levels. As a result, the OSEM-reconstructed PSF profile resembles the true capillary inner diameter.

5. Conclusions

In this study, different X-ray detector schemes for a cone-beam micro-CT system were evaluated. The imaging system was simulated in GATE, introducing seven different detector configurations. Five different scintillators were used, namely, BGO, LSO:Ce, LYSO:Ce, LuAG:Ce, $LaBr_3$:Ce, and two semiconductors (silicon and CZT) as X-ray energy converters. Results were presented in comparison to the CsI:Tl scintillator, currently used in clinical and experimental CBCT systems. Among them, LYSO:Ce, $LaBr_3$:Ce, and LuAG:Ce presented adequate CNRs for all the different spheres' densities, while semiconductors performed well in low-density spine bone tissue. The combination of the examined scintillators with SiPMs attracts an important scientific interest for future experimental setups, since they exhibit comparable performance to the golden standard CsI:Tl. The examined materials, resulting in increased CNRs, could be efficient alternatives for the case of dense breasts.

Author Contributions: Conceptualization, E.K. and C.M.; Data curation, E.K., C.M., N.K., G.F. and I.V.; Formal analysis, E.K., C.M., N.K., G.F. and I.V.; Investigation, E.K., C.M., N.K., G.F. and I.V.; Methodology, E.K., C.M., N.K., G.F. and I.V.; Project administration, C.M. and I.V.; Resources, C.M., G.F. and I.V.; Software, E.K.; Validation, C.M., N.K., G.F. and I.V.; Visualization, E.K., C.M. and I.V.; Writing—original draft, E.K., C.M., N.K., G.F. and I.V.; Writing—review and editing, E.K., C.M., N.K., G.F. and I.V. All authors have read and agreed to the published version of the manuscript.

Funding: This research received no external funding.

Data Availability Statement: Data are contained within the article.

Conflicts of Interest: The authors declare no conflicts of interest.

References

1. O'Connell, A.M.; Marini, T.J.; Kawakyu-O'Connor, D.T. Cone-Beam Breast Computed Tomography: Time for a New Paradigm in Breast Imaging. *J. Clin. Med.* **2021**, *10*, 5135. [CrossRef] [PubMed]
2. Komolafe, T.E.; Zhang, C.; Olagbaju, O.A.; Yuan, G.; Du, Q.; Li, M.; Zheng, J.; Yang, X. Comparison of Diagnostic Test Accuracy of Cone-Beam Breast Computed Tomography and Digital Breast Tomosynthesis for Breast Cancer: A Systematic Review and Meta-Analysis Approach. *Sensors* **2022**, *22*, 3594. [CrossRef] [PubMed]
3. Neubauer, C.; Yilmaz, J.S.; Bronsert, P.; Pichotka, M.; Bamberg, F.; Windfuhr-Blum, M.; Erbes, T.; Neubauer, J. Accuracy of Cone-Beam Computed Tomography, Digital Mammography and Digital Breast Tomosynthesis for Microcalcifications and Margins to Microcalcifications in Breast Specimens. *Sci. Rep.* **2022**, *12*, 17639. [CrossRef] [PubMed]
4. Zhu, Y.; O'Connell, A.M.; Ma, Y.; Liu, A.; Li, H.; Zhang, Y.; Zhang, X.; Ye, Z. Dedicated Breast CT: State of the Art—Part I. Historical Evolution and Technical Aspects. *Eur. Radiol.* **2022**, *32*, 1579–1589. [CrossRef] [PubMed]
5. Dagnall, K.A.; Conley, A.M.; Yoon, L.U.; Rajeev, H.S.; Lee, S.-H.; Choi, J.J. Ytterbium-Doped Cesium Lead Chloride Perovskite as an X-ray Scintillator with High Light Yield. *ACS Omega* **2022**, *7*, 20968–20974. [CrossRef] [PubMed]
6. Mikhailik, V.B.; Kapustyanyk, V.; Tsybulskyi, V.; Rudyk, V.; Kraus, H. Luminescence and Scintillation Properties of CsI: A Potential Cryogenic Scintillator. *Phys. Status Solidi (B)* **2015**, *252*, 804–810. [CrossRef]
7. Zaidi, H. (Ed.) *Molecular Imaging of Small Animals: Instrumentation and Applications*; Springer: New York, NY, USA, 2014; ISBN 978-1-4939-0893-6.
8. García-Jiménez, G.; Cabanelas, P.; González-Caamaño, D.; Alvarez-Pol, H.; Vicente-Pardal, M.A.; Benlliure, J.; Cederkäll, J.; Cortina-Gil, D.; Feijoo-Fontán, M.; Graña-González, A.; et al. Study of Scintillation Properties and Performance of CsI(Tl) Detectors over Time. *Nucl. Instrum. Methods Phys. Res. Sect. A Accel. Spectrometers Detect. Assoc. Equip.* **2024**, *1059*, 169003. [CrossRef]
9. Tian, C.; Liu, S.; Xie, Y.; Guo, L.; Chen, D.; Liu, Y.; Zhong, Z. Study on the Mechanism of Afterglow in CsI: Tl and the Afterglow Suppression in CsI: Tl, Eu. *J. Radioanal. Nucl. Chem.* **2019**, *320*, 123–128. [CrossRef]
10. Lecoq, P. Development of New Scintillators for Medical Applications. *Nucl. Instrum. Methods Phys. Res. Sect. A* **2016**, *809*, 130–139. [CrossRef]
11. Lu, L.; Sun, M.; Wu, T.; Lu, Q.; Chen, B.; Huang, B. All-Inorganic Perovskite Nanocrystals: Next-Generation Scintillation Materials for High-Resolution X-ray Imaging. *Nanoscale Adv.* **2022**, *4*, 680–696. [CrossRef]
12. Danielsson, M.; Persson, M.; Sjölin, M. Photon-Counting X-ray Detectors for CT. *Phys. Med. Biol.* **2021**, *66*, 03TR01. [CrossRef] [PubMed]
13. Noel, A.; Thibault, F. Digital Detectors for Mammography: The Technical Challenges. *Eur. Radiol.* **2004**, *14*, 1990–1998. [CrossRef] [PubMed]
14. Michail, C.; Liaparinos, P.; Kalyvas, N.; Kandarakis, I.; Fountos, G.; Valais, I. Phosphors and Scintillators in Biomedical Imaging. *Crystals* **2024**, *14*, 169. [CrossRef]
15. Shi, L.; Bennett, N.R.; Shapiro, E.; Colbeth, R.E.; Star-Lack, J.; Lu, M.; Wang, A.S. Comparative Study of Dual Energy Cone-Beam CT Using a Dual-Layer Detector and kVp Switching for Material Decomposition. In Proceedings of the Medical Imaging 2020: Physics of Medical Imaging, Houston, TX, USA, 16–19 February 2020; SPIE: Bellingham, WA, USA, 2020; Volume 11312, pp. 481–486.
16. Karpetas, G.E.; Michail, C.M.; Fountos, G.P.; Kalyvas, N.I.; Valais, I.G.; Kandarakis, I.S.; Panayiotakis, G.S. Detective Quantum Efficiency (DQE) in PET Scanners: A Simulation Study. *Appl. Radiat. Isot.* **2017**, *125*, 154–162. [CrossRef]
17. Withers, P.J.; Bouman, C.; Carmignato, S.; Cnudde, V.; Grimaldi, D.; Hagen, C.K.; Maire, E.; Manley, M.; Du Plessis, A.; Stock, S.R. X-ray Computed Tomography. *Nat. Rev. Methods Primers* **2021**, *1*, 18. [CrossRef]

18. van der Sar, S.; Brunner, S.; Schaart, D. X-ray Photon-Counting Using Silicon Photomultiplier-Based Scintillation Detectors at High X-ray Tube Currents. In Proceedings of the SPIE 12031, Medical Imaging 2022: Physics of Medical Imaging, 120310I, San Diego, CA, USA, 4 April 2022; Volume 12031, p. 120310I.
19. Pepin, C.M.; Berard, P.; Perrot, A.-L.; Pepin, C.; Houde, D.; Lecomte, R.; Melcher, C.L.; Dautet, H. Properties of LYSO and Recent LSO Scintillators for Phoswich PET Detectors. *IEEE Trans. Nucl. Sci.* **2004**, *51*, 789–795. [CrossRef]
20. Nikl, M.; Yoshikawa, A.; Kamada, K.; Nejezchleb, K.; Stanek, C.R.; Mares, J.A.; Blazek, K. Development of LuAG-Based Scintillator Crystals—A Review. *Prog. Cryst. Growth Charact. Mater.* **2013**, *59*, 47–72. [CrossRef]
21. Zatcepin, A.; Ziegler, S.I. Detectors in Positron Emission Tomography. *Z. Med. Phys.* **2023**, *33*, 4–12. [CrossRef] [PubMed]
22. Choi, Y.; Kim, K.J.; Park, K.; Kim, Y. A $LaBr_3$(Ce) Detector System with a Simple Spectral Shift Correction Method for Applications in Harsh Environments. *Radiat. Meas.* **2021**, *142*, 106567. [CrossRef]
23. Dey Chaudhuri, S.; Banerjee, D.; Bhattacharjee, T.; Wasim Raja, S.; Acharya, R.; Pujari, P.K. Performance Study of $LaBr_3$:Ce Detectors Coupled to R2083 PM Tube for Energy and Timing Characteristics. *J. Radioanal. Nucl. Chem.* **2020**, *324*, 829–835. [CrossRef]
24. Matsumoto, S.; Ito, A. High-Throughput Production of LuAG-Based Highly Luminescent Thick Film Scintillators for Radiation Detection and Imaging. *Sci. Rep.* **2022**, *12*, 19319. [CrossRef] [PubMed]
25. Kamada, K.; Yanagida, T.; Usuki, Y.; Yoshikawa, A. Detection of Scintillation Light from Pr:$Lu_3Al_5O_{12}$(LuAG) by Gallium Nitride Photodiode. *Nucl. Instrum. Methods Phys. Res. Sect. A* **2009**, *610*, 215–217. [CrossRef]
26. Tseremoglou, S.; Michail, C.; Valais, I.; Ninos, K.; Bakas, A.; Kandarakis, I.; Fountos, G.; Kalyvas, N. Optical Photon Propagation Characteristics and Thickness Optimization of $LaCl_3$:Ce and $LaBr_3$:Ce Crystal Scintillators for Nuclear Medicine Imaging. *Crystals* **2024**, *14*, 24. [CrossRef]
27. Fahrig, R.; Jaffray, D.A.; Sechopoulos, I.; Webster Stayman, J. Stayman Flat-Panel Conebeam CT in the Clinic: History and Current State. *J. Med. Imaging* **2021**, *8*, 052115. [CrossRef] [PubMed]
28. OpenGATE Collaboration. GATE Documentation—GAM Documentation. Available online: https://opengate-python.readthedocs.io/en/0.3.5/ (accessed on 27 February 2024).
29. Mandeville, J.B.; Efthimiou, N.; Weigand-Whittier, J.; Hardy, E.; Knudsen, G.M.; Jørgensen, L.M.; Chen, Y.-C.I. Partial Volume Correction of PET Image Data Using Geometric Transfer Matrices Based on Uniform B-Splines. *Phys. Med. Biol.* **2024**, *69*, 055020. [CrossRef]
30. Vandenberghe, S.; Karakatsanis, N.A.; Akl, M.A.; Maebe, J.; Surti, S.; Dierckx, R.A.; Pryma, D.A.; Nehmeh, S.A.; Bouhali, O.; Karp, J.S. The Potential of a Medium-Cost Long Axial FOV PET System for Nuclear Medicine Departments. *Eur. J. Nucl. Med. Mol. Imaging* **2023**, *50*, 652–660. [CrossRef]
31. Nasr, B.; Villa, M.; Benoit, D.; Visvikis, D.; Bert, J. Monte Carlo Dosimetry Validation for X-ray Guided Endovascular Procedures. *Ann. Vasc. Surg.* **2024**, *99*, 186–192. [CrossRef]
32. Tsalafoutas, I.A.; AlKhazzam, S.; Tsapaki, V.; AlNaemi, H.; Kharita, M.H. Digital Radiography Image Quality Evaluation Using Various Phantoms and Software. *J. Appl. Clin. Med. Phys.* **2022**, *23*, e13823. [CrossRef]
33. Ng, K.-H.; Yeong, C.-H. Imaging Phantoms: Conventional X-ray Imaging Applications. In *The Phantoms of Medical and Health Physics: Devices for Research and Development*; DeWerd, L.A., Kissick, M., Eds.; Springer: New York, NY, USA, 2014; pp. 91–122. ISBN 978-1-4614-8304-5.
34. Kim, H.J.; Rooh, G.; Kim, S. Tl_2LaCl_5 (Ce^{3+}): New Fast and Efficient Scintillator for X- and γ-ray Detection. *J. Lumin.* **2017**, *186*, 219–222. [CrossRef]
35. Meng, F. Development and Improvement of Cerium Activated Gadolinium Gallium Aluminum Garnets Scintillators for Radiation Detectors by Codoping. Ph.D. Dissertation, University of Tennessee, Knoxville, TN, USA, 2015.
36. Jeong, M.; Hammig, M. Development of Hand-Held Coded-Aperture Gamma Ray Imaging System Based on GAGG(Ce) Scintillator Coupled with SiPM Array. *Nucl. Eng. Technol.* **2020**, *52*, 2572–2580. [CrossRef]
37. Venkataraman, R. Semiconductor Detectors. In *Handbook of Radioactivity Analysis*, 4th ed.; L'Annunziata, M.F., Ed.; Academic Press: Cambridge, MA, USA, 2020; pp. 409–491, ISBN 978-0-12-814397-1.
38. Hudson, H.M.; Larkin, R.S. Accelerated Image Reconstruction Using Ordered Subsets of Projection Data. *IEEE Trans. Med. Imaging* **1994**, *13*, 601–609. [CrossRef] [PubMed]
39. Shepp, L.A.; Vardi, Y. Maximum Likelihood Reconstruction for Emission Tomography. *IEEE Trans. Med. Imaging.* **1982**, *1*, 113–122. [CrossRef] [PubMed]
40. Lassot-Buys, M.; Verstraet, R.; Dabli, D.; Moliner, G.; Greffier, J. Task-Based Image Quality Assessment Comparing Classical and Iterative Cone Beam CT Images on Halcyon®. *Diagnostics* **2023**, *13*, 448. [CrossRef] [PubMed]
41. Cherry, S.R.; Sorenson, J.A.; Phelps, M.E. *Physics in Nuclear Medicine*, 4th ed.; Elsevier/Saunders: Philadelphia, PA, USA, 2012.
42. Herman, G.T. *Image Reconstruction from Projections: The Fundamentals of Computed Tomography*; Academic Press: New York, NY, USA, 1980.
43. Baldwin, C.J.; Kelly, E.J.; Batchelor, A.G. The Variation in Breast Density and Its Relationship to Delayed Wound Healing: A Prospective Study of 40 Reduction Mammoplasties. *J. Plast. Reconstr. Aesthetic Surg.* **2010**, *63*, 663–665. [CrossRef] [PubMed]
44. Shannon, F. Characterization of Photon Counting CZT Detectors for Medical X-ray Imaging and Spectroscopy—UW-Madison Libraries. Ph.D. Dissertation, Louisiana State University, Baton Rouge, LA, USA, 2011.

45. Marsh, J.F.; Jorgensen, S.M.; Rundle, D.S.; Vercnocke, A.J.; Leng, S.; Butler, P.H.; McCollough, C.H.; Ritman, E.L. Evaluation of a Photon Counting Medipix3RX Cadmium Zinc Telluride Spectral X-ray Detector. *J. Med. Imaging* **2018**, *5*, 043503. [CrossRef] [PubMed]
46. Le, H.Q.; Ducote, J.L.; Molloi, S. Radiation Dose Reduction Using a CdZnTe-Based Computed Tomography System: Comparison to Flat-Panel Detectors. *Med. Phys.* **2010**, *37*, 1225–1236. [CrossRef] [PubMed]
47. Kalluri, K.S.; Mahd, M.; Glick, S.J. Investigation of Energy Weighting Using an Energy Discriminating Photon Counting Detector for Breast CT. *Med. Phys.* **2013**, *40*, 081923. [CrossRef] [PubMed]
48. Schulze, R.; Heil, U.; Groβ, D.; Bruellmann, D.; Dranischnikow, E.; Schwanecke, U.; Schoemer, E. Artefacts in CBCT: A Review. *Dentomaxillofac. Radiol.* **2011**, *40*, 265–273. [CrossRef] [PubMed]